Journal of Materials Chemistry A

Accepted Manuscript

ROYAL SOCIETY OF CHEMISTRY

www.rsc.org/materialsA

Nitrogen-doped Carbons Prepared from Eutectic Mixtures as Metal-Free Oxygen Reduction Catalysts

Nieves López-Salas,[a] María C. Gutiérrez,[a] Conchi O. Ania,[b] Miguel A. Muñoz-Márquez,[c] M. Luisa Ferrer,[a] and Francisco del Monte[a, *]

[a] *Instituto de Ciencia de Materiales de Madrid-ICMM, Consejo Superior de Investigaciones Científicas-CSIC. Campus de Cantoblanco, 28049-Madrid (Spain)*

[b] *Instituto Nacional del Carbon-INCAR, Consejo Superior de Investigaciones Científicas-CSIC. C/Francisco Pintado Fe, 26, 33011-Oviedo (Spain)*

[c] *CIC Energigune, Parque Tecnológico de Álava. Albert Einstein, 48. 01510-Miñano (Spain)*

Corresponding author:

Francisco del Monte

Tel.: +34 91 3349033

E-mail: delmonte@icmm.csic.es

Abstract

Deep eutectic solvents (DESs) composed of resorcinol, either 2-cyanophenol or 4-cyanophenol, and choline chloride were used for the synthesis of hierarchical nitrogen-doped carbon molecular sieves. Carbons were obtained with high conversions by polycondensation of resorcinol and either 2-cyanophenol or 4-cyanophenol with formaldehyde, and subsequent carbonization at 800 °C in nitrogen atmosphere. The nitrogen content was ca. 2.4 wt%, revealing an excellent nitrogen-doping efficiency for cyanophenol derivatives when used in the form of DES. The use of either 2-cyanophenol or 4-cyanophenol modified the contribution of quaternary-N_{valley} groups in the resulting carbons, being larger in carbons coming from 4-cyanophenol than in those coming from 2-cyanophenol. The hierarchical porous structure was composed of micro-, meso- and macropores, and the diameter distribution of mesopores was also related to the use of either 2-cyanophenol or 4-cyanophenol. These structural and compositional differences were critical for the use of the resulting hierarchical nitrogen-doped carbons as efficient metal-free electrocatalysts. In particular, the carbons coming 4-cyanophenol proved particularly effective in the direct reduction of oxygen to OH^- (H_2O in acidic solution) through a four-electron ($4e^-$) process with high catalytic activity and selectivity, and longer stability and stronger tolerance to crossover effects than platinum-based electrocatalysts.

Introduction

Fuel cells – based on the electrocatalytic oxidation of a fuel (e.g. hydrogen or methanol) at the anode and the electro-catalytic reduction of an oxidizing agent (typically oxygen) at the cathode – have become a promising alternative as sustainable electrochemical energy conversion systems.[1] However, the use of expensive platinum-based electrocatalysts for the oxygen reduction reaction (ORR) is a serious drawback that actually limits the competitiveness of this sort of devices and hence, their large-scale application. Within this context, the development of low-platinum, platinum-free and even metal-free electrodes has been the subject of research of numerous works.[2, 3] Among them, heteroatom-doped carbons have proved particularly effective as efficient metal-free electrocatalysts, with enhanced catalytic activity and selectivity, longer stability and stronger tolerance to crossover effects than platinum for oxygen reduction in alkaline media.[4] Nitrogen-doped carbons are by far the most abundantly investigated,[5, 6] but boron- and phosphorous-doped carbons have been widely investigated as well.[7, 8] These works have demonstrated that breaking the electroneutrality of graphitic materials by doping with elements, which have larger (e.g., nitrogen) or smaller (e.g., phosphorus or boron) electronegativity than carbon, might be an important factor for promoting ORR activity because the presence of positively charged sites favours side-on O_2 adsorption and ultimately facilitates the direct reduction of oxygen to OH^- (H_2O in acidic solution) through a four-electron ($4e^-$) process.[9]

Interestingly, the origin of the oxygen reduction reaction (ORR) activity in nitrogen-doped carbons remains elusive and is still a topic of debate. This controversy is fed by the general assumption that the ORR activity is monotonously determined by the type or content of N-containing structures. However, there is no method that could recognize the individual contribution from a specific N-group to the ORR process so a more realistic view should consider that the observed ORR activity represents a collective property. Thus, pyrrolic-N was present in some ORR-active NPCs but some other authors reported on their null contribution to ORR.[10, 11] More agreement exists with regard to the role played by pyridinic-N[12, 13] or quaternary-N,[14, 15] in a first stage ascribing the activity to either one[16, 17] or the other,[18, 19] and more recently to the combined action of both.[20, 21, 22] Interestingly, recent works studying the role played by quaternary-N are now distinguishing between quaternary-N center and quaternary-N valley. Thus, theoretical models have predicted that quaternary-N valley sites are more active than pyridinic ones, and these more than quaternary-N center sites in nitrogen doped graphene nanoribbons,[23] and this prediction was actually confirmed by experimental work carried out with nitrogen doped carbon nanotubes (N-doped CNTs).[20] Nonetheless, one should also keep in mind that the higher the surface area the larger the functionalization, so

control on the textural properties is critical as well.

Thus, number of synthetic strategies has been used for preparation of nitrogen porous carbons (NPCs), via either carbon post-treatment with nitrogen-rich reagents– e.g. ammonia, amines or urea, among others – or using nitrogen-rich compounds – e.g. acetonitrile, pyrrole or polyaniline, among others – as carbon precursors. With regard to this latter case, the use of ionic liquids (ILs) based on cyanide compounds provided – with the aid of soft or hard templates – NPCs with extraordinary high nitrogen contents. Yet, the challenge of this approach is to obtain carbons with high yields. Moreover, attention has been paid to the design of greener synthetic approaches – e.g. upon the use of natural/renewable resources as raw materials and in the absence of harsh solvents – capable to further enhance the sustainable features of NPC-based systems as compared to metal-based ones. Within this context, the hydrothermal carbonization of biomass[24] and the direct carbonization of different biomolecules[25, 26, 27] – e.g. proteins and glycoproteins, nucleobases, etc. – and biopolymers[28, 29] – e.g. chitosan, aminated tannins and glycoproteins – have proved quite effective for the preparation of NPCs.

More recently, the use of eutectic mixtures as carbon precursors via polycondensation with formaldehyde has also offered an interesting alternative for NPCs preparation. Eutectics are molecular complexes typically formed between quaternary ammonium salts and hydrogen-bond donors. The charge delocalization that occurs through hydrogen bonding between the halide anion and the hydrogen-donor moiety is responsible for the decrease in the melting point of the mixture relative to the melting points of the individual components. The eutectic mixture of choline chloride and urea – first described by Abbott and co-workers as deep eutectic solvents (DESs) – is most likely the most studied one.[30] More recently, eutectics with a particular composition and/or physico-chemical behaviour have received different names – e.g. low-melting eutectic mixtures of sugar, urea, and salts first described by König and co-workers; [31] natural deep eutectic solvents (NADES) by Choi et al.;[32] and low-transition–temperature mixtures (LTTMs) by Kroon and co-workers[33] – but we will just use the DES acronym in this work. Within the context of this work, DES-assisted syntheses may provide both sustainability – (1) eutectic components may originally come from natural/renewable resources and (2) eutectic mixtures may act, during the synthetic process, as all-in-one solvent-template-reactant systems with the subsequent economy of reagents[34, 35] – as well as compositional versatility – there is a wide number of nitrogen-rich components capable to form eutectic mixtures that, eventually, could introduce different functionalities at the porous surface of the resulting carbons.

Herein, we have used DES composed of resorcinol (R), either 2-cyanophenol (2CP) or 4-cyanophenol (4CP), and choline chloride (C) to obtain NPCs upon polycondensation with formaldehyde (F). DES formation was studied by ^{1}H-NMR spectroscopy and by differential scanning calorimetry (DSC). The use of either 2CP or 4CP aimed tailoring the textural properties of the resulting carbons – as consequence of their different reactivity in polycondensation reactions – and/or to introduce different functionalities on the porous surface. Resins resulting after polycondensation were studied by ^{13}C-NMR and FTIR spectroscopies. Carbons resulting after resins carbonization were studied by nitrogen (N_2) and carbon dioxide (CO_2) adsorption/desorption isotherms. Moreover, nitrogen functionalization at the carbons was studied by X-ray photoelectron spectroscopy (XPS) and elemental chemical analysis (ECA). Scanning and transmission electron microscopies (SEM and TEM, respectively) also provided useful insights of the carbons morphology. The ORR activity was investigated for carbons obtained from both 2CP and 4CP, hence exhibiting different textural properties and nitrogen functionalizations.

Results and Discussion

R2CPC-DES and R4CPC-DES were obtained by physical mixing of the individual components – e.g. R, 2CP and C, and R, 4CP and C, respectively – in a 1:1:1 molar ratio and posterior thermal treatment at 90°C overnight. The molten mixtures remained in the liquid phase when returned to room temperature. R2CPC-DES and R4CPC-DES were investigated by differential scanning calorimetry (DSC). Neither melting temperature (T_m) nor crystallization temperature (T_c) was displayed in the DSC trace of any of the studied DESs (Fig. 1) which is a common feature observed for non-easily crystallizable ILs and DESs. Thus, the DSC scans only displayed the glass transition temperatures (T_g) of R2CPC-DES and R4CPC-DES at -64 and -66°C, respectively (Fig. 1).[36] The formation of ternary H-bond complexes was also confirmed by the upfield chemical shift of the signals ascribed to every DES component – e.g. R, 2CP and C in R2CPC-DES, and R, 4CP, and C in R4CPC-DES – in the ^{1}H NMR spectra of the respective mixtures (Fig. S1, Tables S1 and S2 in ESI).[37, 38, 39] This result disregarded the hypothetical case where one of the precursors is just dissolved in the respective binary DES because, if so, the chemical shifts of this dissolved precursor would be closer to those of its individual components.

The polycondensation of R2CPC-DES and R4CPC-DES was carried out in basic conditions (Na_2CO_3) by the addition of an aqueous solution of F (37 wt%). This DES dilution – e.g. to about 53 wt%, respectively – promoted a partial rupture of the ion-hydrogen-bond-donor supramolecular complexes (Fig. S2 in ESI) that makes R, 2CP and 4CP available for condensation, and initiates the segregation between the condensed phase and the non-

condensed compounds that ultimately determines the morphology of the resulting materials.[34] The extension in which 2CP and 4CP co-condensate with R was studied in detail by FTIR and solid-state ^{13}C CPMAS NMR spectroscopies. For this purpose and as described elsewhere,[38] resins (Fig. S3 in ESI) were first thoroughly washed with abundant water to eliminate any non-condensed reagent (Fig. S4 in ESI). The FTIR spectrum of the washed resins (Fig. 2) revealed the formation of a significant number of linkages between R rings by the presence of bands assigned to methylene (C–H stretching and bending modes at ca. 2935 and 1475 cm^{-1}, respectively) and to methylene oxide groups (C–O benzyl ether groups at about 1225 and 1095 cm^{-1}).[40] Meanwhile, the co-condensation of R with 2CP and 4CP was confirmed by the presence of the band at ca. 2225 cm^{-1} that correspond to the stretching vibration of C-N in the cyano group.[41, 42, 43]

Co-condensation between R and 2CP, and R and 4CP was also confirmed by solid state ^{13}C CPMAS NMR spectroscopy – i.e. see the peaks at 152 and 157 ppm for R2CPC resins, and at 152 and 160 ppm for R4CPC resins corresponding to aromatic carbons bearing hydroxyl and cyano groups, respectively (Fig. 3). Moreover, peaks at 53 ppm, and at 31 and 24 ppm were ascribed to methylene ether (e.g., CH_2–O–CH_2) and methylene (e.g., CH_2) bridges, respectively. The peak at 131-132 ppm corresponded to non-substituted aromatic carbons in meta positions. Different types of CH_2 bridges can be distinguished depending on the chemical shift.[44, 45] Thus, the most common 4–4' methylene bridge has been typically assigned to signals at 30–38 ppm, and the less common 2–4' methylene bridges to signals at 22–30 ppm. The integration of the sum of the signals at 152-160 ppm versus the sum of the signals at 53, 31 and 24 ppm was higher for R2CPC than for R4CPC resins. The enhanced degree of condensation found for R2CPC resins was corroborated by the intensity of the peak at 118 ppm assigned to aromatic carbons bearing CH_2 groups in all ortho- positions relative to the two phenolic OHs that result after condensation. Both precursors would tend to form linear rather than cross-linked polymers unless one uses them as additional precursors besides R, as in our case. Nonetheless, it is worth noting that the positions at the aromatic ring deactivated by the presence of cyano groups are different in 2CP than in 4CP. In the former case, the cyano group blocks one of the ortho-positions susceptible to nucleophilic substitution and only the positions at C4 and C6 of the aromatic ring remain available for condensation. In the latter case, the cyano group blocks the meta-position thus remaining both ortho-positions – i.e. at C2 and C6 of the aromatic ring – available for condensation. Under these circumstances, it seems plausible that co-condensation is favoured in 2CP – more so than in 4CP – because of steric hindrance. It is worth noting that condensation positions in 2CP are located at the aromatic

ring opposite to the aromatic-ring-pending groups – e.g. cyano and hydroxyl – whereas in 4CP these positions are alternated along the aromatic ring.

R2CPC and R4CPC resins were thermally treated at 800 °C in N_2 atmosphere for the formation of NPCs with high conversions (Table 1)[38] – i.e. at least, in range to those reported for previous DES-assisted condensations – as anticipated by ^{13}C NMR spectroscopy. SEM micrographs revealed the formation of an aggregates-of-particles-like morphology,[46, 47] consequence of the phase-separation process that typically occurs in DES-assisted polycondensations (Fig. 4).

The textural properties of the carbons were also studied by N_2 and CO_2 adsorption-desorption isotherms at –196 and 0 °C, respectively. With regard to the N_2 adsorption isotherms, both materials display a type IV isotherm (Fig. 5a) with a sharp knee at low relative pressures that indicates the presence of a narrow micropore size distribution – e.g. typical of carbon molecular sieves – and prominent H2 hysteresis loops in the desorption branch at relative pressures above ca. 0.7 that revealed the presence of mesopores. CO_2 adsorption–desorption isotherms revealed the good sorption capabilities of R2CPC and R4CPC carbons – i.e. with up to 3.75 mmol/g at 0 °C for both samples, see Fig. 5b) and confirmed the presence of narrow microporosity (see W_o and L in Table 2). Both R2CPC and R4CPC carbons also exhibited similar S_{BET}, total micropore volume, and average micropore diameters – e.g. 668 and 660 m^2/g, 214 and 0.218 cm^3/g, and 0.66 and 0.64 nm, respectively (Fig. S5 in ESI). The main difference in the textural features of the carbons resides the mesoporous network. Thus, the position of the hysteresis loop in the N_2 adsorption isotherms was nearly the same in both samples, whereas the desorption branch of the R2CPC isotherm showed a stepped pattern with a curvature – i.e. inflection point – at $p/p_0 \sim 0.85$ that was not observed in the desorption branch of the R4CPC isotherm. This stepped adsorption feature is characteristic of systems with pore blocking effects derived from the presence of a constrained pore structure where wide pores are connected through narrow openings and has also been described for other materials – e.g. Vycor glass,[48] porous silicon layers,[49] mesoporous silica,[50] and carbon xerogels.[51] This is why the mesopore diameters differed between R2CPC and R4CPC (see Figures 5c and S5) but not the pore volumes (Table 2). We further corroborated this issue by the analysis of the pore size distribution using the 2D-NLDFT-HS model applied to the desorption branch of the isotherm (Fig. 5c, and Fig. S5a in ESI). The model fitted relatively well the experimental data in the whole range of relative pressures. In both samples, the PSD showed a bimodal distribution of the mesoporosity – with a main peak located at ca. 10 nm and a shoulder at 20 nm – being the distribution broader in the R4CPC case. The narrow pore openings connecting the large mesopores in R2CPC were also evident in the hump appearing

at the lower range of pore-size-distribution plot (Figure 5c). The analysis of the PSD by classical methods – e.g. BJH, also applied to the desorption branch – provided data with a similar pattern than that obtained by 2D NLDFT-HS (Fig. S5b in ESI) and confirmed the accuracy of the analysis. Interestingly, the preferred formation of large mesopores in R4CPC – more so than in R2CP – could be related to the condensation degree observed above for 2CP and R, than for 4CP and R.

Besides morphology control, the use of DES-assisted co-condensations aimed introducing certain functionalities in the resulting carbon. The nitrogen content was ca. 2.3-2.4 wt% according to ECA data (Table 1). We further studied the nitrogen functionalities of R2CPC and R4CPC carbons by XPS (Fig. 6 and Table 3). Up to five types of nitrogen (pyridinic-N at 398.1 ± 0.3 eV, pyrrolidonic-N at 399.2 ± 0.3 eV, pyrrolic-N or pyridonic-N at 400.4 ± 0.3 eV, quaternary-N at 401.2 ± 0.5 eV and oxidized-N at 403–405 eV) are typically distinguished in nitrogen-doped carbons.[52, 53] As described elsewhere,[20] we also represented quaternary-N by two peaks, one at around 401.0 eV that is typically referred to as graphitic nitrogen and here denoted as quaternary-N_{center} and a second one at around 402.0 eV which we refer to as quaternary-N_{valley}. In our case, the contribution of pyrrolidonic-N type was negligible while those of oxidized-N, pyrrolic-N or pyridonic-N, pyridinic-N, and even quaternary-N_{center} were quite similar in both R2CPC and R4CPC carbons. Differences between R2CPC and R4CPC carbons were only found in the quaternary-N_{valley} contribution, ca. 2-fold larger in the latter case than in the former one.

The ORR catalytic performance of R2CPC and R4CPC carbons – at a constant active mass loading – was first investigated by cyclic voltammetry (CV) in N_2- and O_2-saturated 0.1 M KOH solutions (Fig. 7). The CV of a commercial platinum-carbon black catalyst (Pt/C, 20% Pt loading) was also performed for comparison (Fig. S6a). The voltammograms of R2CPC and R4CPC carbons showed none obvious redox peak when the electrolyte was N_2-saturated. Meanwhile, a cathodic peak appeared in both carbons – centred at -0.20 V for R2CPC ones and at -0.24 V for R4CPC ones (versus Ag/AgCl/KCl reference electrode, onset value extracted from CV in O_2 saturated 0.1M KOH) – when the electrolyte was O_2-saturated. The voltammograms were quasi-rectangular-shaped in both cases as a result of the electrochemical double layer formed upon ions adsorption on the pore surface of microporous carbons.

The ORR activity was further evaluated using linear sweep voltammetry (LSV) measurements on a rotating-disk electrode (RDE) at a rotation rate of up to 2000 rpm (Fig. 7). The LSV profile of Pt/C (20% Pt loading) was also studied for comparison (Fig. S6b). We observed clear differences between both the onset potential and the limiting current density of R2CPC and R4CPC carbons with less positive onset potentials and lower limiting current

densities ranging from R4CPC to R2CPC up to the commercial Pt/C catalyst (Fig. 8a). The Koutecky–Levich plots (K-L) plots (J^{-1} vs $\omega^{-1/2}$) at -250 mV exhibited good linearity for both carbons, indicating that current was mainly kinetically controlled (Fig. 8b).[54] At this stage, it is worth mentioning that the rate constants determined by the K-L analysis of RDE voltammetric data may reflect apparent rate constants and not true standard ones for porous electrodes where the electroactive surface area differs from the geometric one.[55] Thus, it seems that when the ratio between the electroactive surface area and the geometric area of the current collector (ψ) is below 1, the reaction proceeds at higher overpotentials whereas the opposite situation is found when ψ is above 1. Meanwhile and provided the hydrodynamic requirements remain valid, the diffusion limited flux seemed to be independent of ψ and the determination of *n* using the K-L analysis is not affected.[56] Interestingly, the transferred electron number (*n*) obtained from the slope of the K-L plots of R2CPC and R4CPC carbons revealed that the four-electron-transfer reaction that reduces oxygen directly to OH^- only occurs in R4CPC carbons. Thus, while *n* for R2CPC carbons remained around 2.5 all over the studied range of potentials, it experienced a significant increase for R4CPC carbons from -400 to -300 V where the figure was similar to that found for Pt/C – e.g. 3.7 (Fig. 8c).

At this stage, the question that arises is why the four-electron-transfer reaction prevailed over the two-electron-transfer one in R4CPC carbons but not in R2CPC ones. As mentioned in the introduction, the ORR activity in N-doped carbons is typically ascribed to the type or content of N-containing structures for materials exhibiting similar surface areas. In our case, not only the surface areas but also some other textural features at the micropore range – e.g. micropore volume and diameter – of R2CPC and R4CPC carbons were quite similar (Table 2) so we could hypothesized that N-doped carbons richer in quaternary-N_{valley} than in quaternary-N_{center} – e.g. R4CPC ones – favour the four-electron-transfer reaction, as predicted for N-doped graphene[23] and experimentally observed for N-doped CNTs.[20] Nonetheless, one could also wonder whether the presence of large mesopores – i.e. larger in R4CPC than in R2CPC carbons – could also play a role by favouring electrolyte diffusion and hence, accessibility to the electroactive species on the porous surface.

We finally studied the methanol tolerance and the stability of R4CPC carbons (Fig. 8d and Fig. S7). The former is an important issue for cathode materials in low-temperature fuel cells and also an obvious shortcoming of Pt-based catalysts. For this reason, the methanol crossover effect was also evaluated on the commercial Pt/C described above. In this case, methanol addition promoted a sharp drop of the current response of Pt/C to ca. 30 % of the original figure while the CV exhibited an intense peak due to methanol oxidation. In contrast, the current response of R4CPC carbon after methanol addition experienced a smooth decrease,

maintaining more than 90 % of the original current 2000 seconds after addition. The LSV curves performed after the addition of methanol and the stability test were in agreement with this regard (Fig. S7). Finally and in terms of stability, it is worth noting that current attenuation of the R4CPC carbon was ca. 12 % after 20000 seconds situating the stability of this N-doped carbon in range to those found for other N-doped carbons.[57, 58, 59, 60, 61]

Conclusions

In summary, we have described a template-free approach based on the use of eutectic mixtures containing either 2CP or 4CP as nitrogen-rich precursors for the preparation of N-doped porous carbons useful as metal-free oxygen reduction catalysts. The use of 2CP or 4CP as precursors provided interesting features to the resulting carbons in both compositional and structural terms. In particular, we have observed a larger contribution of quaternary-N_{valley} groups in R4CPC than in R2CPC carbons. This behaviour agreed with that described in previous works where the highest activity for the four-electron-transfer reaction is assigned to quaternary-N_{valley} groups, followed by pyridinic-N ones, and finally by quaternary-N_{center} ones. Nonetheless, one might also consider in our case whether accessibility to the functionalized surface could also play a role in the ORR activity. Actually, large mesopores of ca. 18-20 nm in diameter prevailed over those of 8.5-10 nm in R4CPC carbons while the opposite occurred in R2CPC ones.

Experimental Section

Materials

Resorcinol (R), 2-cyanophenol (2CP), 4-cyanophenol (2CP), choline chloride (C), formaldehyde (F, 37 wt% in aqueous solution), and Nafion 117 (5 wt%) were purchased from Sigma-Aldrich and used as received. Water was distilled and deionized.

Synthesis

DESs were obtained by physical mixing of the individual components and posterior thermal treatment at 90 °C overnight. R2CPC-DES was prepared by mixing R, 2CP and C, while R4CPC-DES was prepared by mixing R, 4CP and C, using in both cases a 1:1:1 molar ratio.

Polycondensations were carried out upon the addition of F (0.595 ml, 37 wt% in aqueous solution) to 737 mg of either R2CPC-DES or R4CPC-DES so that the molar ratio of F to precursor – e.g. R+2CP or R+4CP – was 2. The mixture was homogenized upon gently stirring and then 0.061 ml of Na_2CO_3 (140 mg/ml) was added as the basic catalyst. Afterward, samples were thermally treated at 60 °C over 1 day and then at 90 °C over the following 6 days. The

resulting resins were washed before carbonization at 800 °C over 4 hours (the heating ramp was 1.0 °C/min) in a nitrogen atmosphere.

Sample characterization

DESs were studied by ^{1}H NMR spectroscopy using a Bruker spectrometer DRX-500. DESs were placed in capillary tubes, using deuterated dimethyl sulfoxide (DMSO) as an external reference. Differential scanning calorimetry (DSC) was performed with a TA Instruments Model DSC Q-100 system, under a nitrogen atmosphere. The samples were placed in an aluminium pan in a sealed furnace, stabilized at 50 °C over 30 min, and then cooled to -90 °C before heating at rates of 1 and 10 °C/min. Fourier transform infrared (FTIR) spectroscopy of resins was performed in a FTIR spectrometer (Bruker Model IFS60v). Solid-state ^{13}C-CPMAS-NMR spectra of resins were obtained using a Bruker Model AV-400-WB spectrometer, by applying a standard cross-polarization pulse sequence. Elemental chemical analysis (ECA) of resins was performed in an LECO Elemental Analyzer CHNS 932. Scanning electron microscopy (SEM) was performed using a SEM Hitachi S-3000N system. Transmission electron microscopy (TEM) was performed using a JEOL 2000 system operating at 200 keV.

X-ray Photoelectron Spectroscopy (XPS) was performed with a SPECS Phoibos 150 spectrometer and a non-monochromatic Mg K_{α} source (hv = 1253.6 eV). Samples were mounted in molybdenum sample plates using adhesive carbon tape and inserted into the XPS vacuum system through a fast entry chamber. The base pressure of the system was in the 10^{-10} mbar range. Survey spectra in the 0 to 1100 eV range were acquired to successfully monitor the sample purity. High resolution scans of the N1*s* and C1*s* photoemission lines were acquired at 200 W, 20 eV pass energy, and 0.1 eV energy step. X-ray beam intensity was tested in reference samples to avoid X-ray induced damage. The spectrometer was calibrated using three reference samples (Au, Ag and Cu) that are used to determine the linear expansion of the energy scale. The C1*s* peak was used for binding energy calibration as internal reference in the sample – i.e. note that for these graphitic materials that undergo thermal treatments there is a narrow graphitic peak at 284.6 eV (FWHM = 1.1 eV) which is followed by a broader peak shifted by +0.45 eV (FWHM = 2.2 eV) that arises from regions of defective graphitic structure.[62] The measured photoemission lines were fitted using the CasaXPS software. Voigt functions (70% Gaussian and 30% Lorentzian) were used in the fits to determine the peak positions, intensity and FWHM. The fitting parameters were obtained using a Levenberg–Marquardt optimization algorithm starting from different initial guess parameters that always led to the same result. A Shirley background was subtracted from experimental data and satellite lines from the non-monochromatic X-ray source were removed. Thus, the ratio between the different N-functionalizations in the N 1*s* peak was obtained for the measured samples.

High-resolution nitrogen adsorption–desorption isotherm measurements at -196 • C were measured in an ASAP 2020 (Micromeritics) volumetric analyzed on samples previously degassed under dynamic vacuum (ca. 10-5 Torr) at 100 • C for 17 hours. The instrument was equipped with a molecular drag vacuum pump and three pressure transducers (0.0133, 1.33 and 133 kPa, uncertainty within 0.15% of reading) to enhance the sensitivity in the low-pressure range. Strict analysis conditions were programmed during the gas adsorption measurements to ensure equilibrium data, thus the average elapsed time for each isotherm of the isotherms was 90-120 h, with over 100 equilibrium points. Each isotherm measurement was performed in duplicate to guarantee the accuracy of the experiments (error was below 0.1%) and to obtain reproducible data. Ultrahigh purity nitrogen (i.e., 99.9992%) was supplied by Air Products. The isotherms were used to calculate the specific surface area using the Brunauer-Emmett-Teller theory, S_{BET}, total pore volume, V_{TOTAL}, and micropore volumes using the Dubinin-Radushkevich equation.[63] The PSD analysis in the mesopore range was performed using the BJH formulism applied to the desorption branch, and the full micro-mesopore size distribution was calculated using the 2D-NLDFT-HS model for carbons with energetically heterogeneous and geometrically corrugated pore walls.[64]

The ORR activity was investigated using an Autolab PGSTAT302N with a three-electrode setup. A platinum mesh and an Ag/AgCl/KCl (3M) were used as counter and reference electrodes, respectively. The active material was prepared in form of slurry by mixing either R2CPC or R4CPC carbon in powdered form (5 mg), ethanol (170 µL) and Nafion 117 (47.5 µL). The glassy carbon rotating-disk-working electrode (4 mm in diameter) was polished and coated twice – by drop casting – with 3.5 µL of the slurry. All electrochemical measurements, including cyclic voltammograms (CV), rotating-disk electrode voltammograms (LSV) and chronoamperometry, were performed at room temperature in 0.1 M KOH solutions, previously purged with high purity either nitrogen or oxygen for at least 30 min. Both CV and LSV were recorded at 10 mV/s scan rate and the potential window ranged from 0.0 to -1.0 V. Chronoamperometry was performed at 1600 rpm in O_2 saturated 0.1M KOH.

Bibliography

1 B. C. H. Steele, A. Heinzel, "Materials for fuel-cell technologies" *Nature* **2001**, *414*, 345–352.

2 R. Bashyam, P. Zelenay, "A class of non-precious metal composite catalysts for fuel cells" *Nature* **2006**, *443*, 63–66.

3 H. A. Gasteiger, N. M Marković, "Just a Dream—or Future Reality?" *Science* **2009**, *324*, 48–49.

[4] For a recent review, see: D.-W. Wang, D. Su, "Heterogeneous nanocarbon materials for oxygen reduction reaction" *Energy Environ. Sci.* **2014**, *7*, 576.

[5] K. Gong, F. Du, Z. Xia, M. Durstock, L. Dai, "Nitrogen-Doped Carbon Nanotube Arrays with High Electrocatalytic Activity for Oxygen Reduction" *Science* **2009**, *323*, 760–764.

[6] L. Qu, Y. Liu, J.-B. Baek, L. Dai, "Nitrogen-Doped Graphene as Efficient Metal-Free Electrocatalyst for Oxygen Reduction in Fuel Cells" *ACS Nano* **2010**, *4*, 1321–1326.

[7] Z.-W. Liu, F. Peng, H.-J. Wang, H. Yu, W.-X. Zheng, J. Yang, "Phosphorus-Doped Graphite Layers with High Electrocatalytic Activity for the O2 Reduction in an Alkaline Medium" *Angew. Chem. Int. Ed.* **2011**, *50*, 3257 – 3261; *Angew. Chem.* **2011**, *123*, 3315 – 3319.

[8] L. Yang, S. Jiang, Y. Zhao, L. Zhu, S. Chen, X. Wang, Q. Wu, J. Ma, Y. Ma, Z. Hu, "Boron-Doped Carbon Nanotubes as Metal-Free Electrocatalysts for the Oxygen Reduction Reaction" *Angew. Chem. Int. Ed.* **2011**, *50*, 7132–7135; *Angew. Chem.* **2011**, *123*, 7270–7273.

[9] L. P. Zhang, Z. H. Xia, "Mechanisms of Oxygen Reduction Reaction on Nitrogen-Doped Graphene for Fuel Cells" *J. Phys. Chem. C* **2011**, *115*, 11170 – 11176.

[10] J. D. Wiggins-Camacho, K. J. Stevenson, "Mechanistic discussion of the oxygen reduction reaction at nitrogen-doped carbon nanotubes." *J. Phys. Chem. C* **2011**, *115*, 20002.

[11] K. Artyushkova, S. Pylypenko, T. S. Olson, J. E. Fulghum, P. Atanassov, "Predictive modeling of electrocatalyst structure based on structure-to-property correlations of X-ray photoelectron spectroscopic and electrochemical measurements." *Langmuir* **2008**, *24*, 9082.

[12] R. A. Sidik, A. B. Anderson, N. P. Subramanian, S. P. Kumaraguru, B. N. Popov, "O_2 reduction on graphite and nitrogen-doped graphite: experiment and theory." *J. Phys. Chem. B* **2006**, *110*, 1787.

[13] K. Y. Park, J. H. Jang, J. E. Hong, Y. U. Kwon, "Mesoporous Thin Films of Nitrogen-Doped Carbon with Electrocatalytic Properties" *J. Phys. Chem. C* **2012**, *116*, 16848.

[14] D. S. Geng, Y. Chen, Y. G. Chen, Y. L. Li, R. Y. Li, X. L. Sun, S. Y. Ye, S. Knights, "High oxygen-reduction activity and durability of nitrogen-doped graphene" *Energy Environ. Sci.* **2011**, *4*, 760.

[15] A. Morozan, P. Jegou, M. Pinault, S. Campidelli, B. Jousselme, S. Palacin, "Metal-Free Nitrogen-Containing Carbon Nanotubes Prepared from Triazole and Tetrazole Derivatives Show High Electrocatalytic Activity towards the Oxygen Reduction Reaction in Alkaline Media" *ChemSusChem* **2012**, *5*, 647.

[16] S. Shanmugam, T. Osaka, "Efficient electrocatalytic oxygen reduction over metal free-nitrogen doped carbon nanocapsules" *Chem. Commun.* **2011**, *47*, 4463–4465

[17] L. Qu, Y. Liu, J. B. Baek, L. Dai, "Nitrogen-Doped Graphene as Efficient Metal-Free Electrocatalyst for Oxygen Reduction in Fuel Cells" *ACS Nano* **2010**, *4*, 1321–1326.

[18] H. Niwa, K. Horiba, Y. Harada, M. Oshima, T. Ikeda, K. Terakura, J. Ozaki, S. Miyata, "X-ray absorption analysis of nitrogen contribution to oxygen reduction reaction in carbon alloy cathode catalysts for polymer electrolyte fuel cells" *J. Power Sources* **2009**, *187*, 93–97

[19] T. C. Nagaiah, S. Kundu, M. Bron, M. Muhler, W. Schuhmann, "Nitrogen-doped carbon nanotubes as a cathode catalyst for the oxygen reduction reaction in alkaline medium" *Electrochem. Commun.* **2010**, *12*, 338–341

[20] T. Sharifi, G. Hu, X. E. Jia, T. Wagberg, "Formation of Active Sites for Oxygen Reduction Reactions by Transformation of Nitrogen Functionalities in Nitrogen-Doped Carbon Nanotubes." *ACS Nano* **2012**, *6*, 8904.

[21] L. F. Lai, J. R. Potts, D. Zhan, L. Wang, C. K. Poh, C. H. Tang, H. Gong, Z. X. Shen, L. Y. Jianyi, R. S. Ruoff, "Exploration of the active center structure of nitrogen-doped graphene-based catalysts for oxygen reduction reaction" *Energy Environ. Sci.* **2012**, *5*, 7936.

[22] A. Zhao, J. Masa, M. Muhler, W. Schuhmann, W. Xi, "N-doped carbon synthesized from N-containing polymers as metal-free catalysts for the oxygen reduction under alkaline conditions." *Electrochim. Acta* **2013**, *98*, 139-145.

[23] H. Kim, K. Lee, S. I. Woo, Y. Jung, "On the Mechanism of Enhanced Oxygen Reduction Reaction in Nitrogen-Doped Graphene Nanoribbons." *Phys. Chem. Chem. Phys.* **2011**, *13*, 17505–17510.

[24] N Brun, S. A. Wohlgemuth, P. Osiceanu, M. M. Titirici, "Original design of nitrogen-doped carbon aerogels from sustainable precursors: application as metal-free oxygen reduction catalysts." *Green Chem.* **2013**, *15*, 2514.

[25] N. Baccile, M. Antonietti, M. M. Titirici, "One-Step Hydrothermal Synthesis of Nitrogen-Doped Nanocarbons: Albumine Directing the Carbonization of Glucose" *ChemSusChem* **2010**, *3*, 246–253.

[26] R. J. White, M. Antonietti, M. M. Titirici, "Naturally inspired nitrogen doped porous carbon" *J. Mater. Chem.* **2009**, *19*, 8645–8650

[27] W. Yang, T. Fellinger, M. Antonietti, "Efficient Metal-Free Oxygen Reduction in Alkaline Medium on High-Surface-Area Mesoporous Nitrogen-Doped Carbons Made from Ionic Liquids and Nucleobases" *J. Am. Chem. Soc.* **2011**, *133*, 206–209.

[28] F. Braghiroli, V. Fierro, M. Izquierdo, J. Parmentier, A. Pizzi, A. Celzard, "Nitrogen-doped carbon materials produced from hydrothermally treated tannin" *Carbon* **2012**, *50*, 5411–5420.

[29] L. Zhao, N. Baccile, S. Gross, Y. Zhang, W. Wei, Y. Sun, M. Antonietti, M. M. Titirici, "Sustainable nitrogen-doped carbonaceous materials from biomass derivatives" *Carbon* **2010**, *48*, 3778–3787.

[30] A. P. Abbott, G. Capper, D. L. Davies, R. K. Rasheed, V. Tambyrajah, "Novel solvent properties of choline chloride/urea mixtures" *Chem. Commun.* **2003**, 70–71.

[31] G. Imperato, E. Eibler, J. Niedermaier, B. König, "Low-melting sugar–urea–salt mixtures as solvents for Diels–Alder reactions" *Chem. Commun.* **2005,** 1170-1172.

[32] Y. H. Choi, J. van Spronsen, Y. Dai, M. Verberne, F. Hollmann, I. W. C. E. Arends, G.-J. Witkamp, R. Verpoorte, "Are Natural Deep Eutectic Solvents the Missing Link in Understanding Cellular Metabolism and Physiology?" *Plant Physiology* **2011**, *156,* 1701–1705.

[33] M. Francisco, A. van den Bruinhorst, M. C. Kroon, "Low-Transition-Temperature Mixtures (LTTMs): A New Generation of Designer Solvents" *Angew. Chem.* **2013**, *52*, 3074–3085.

[34] F. del Monte, D. Carriazo, M. C. Serrano, M. C. Gutiérrez, M. L. Ferrer, "Deep Eutectic Solvents in Polymerizations: A Greener Alternative to Conventional Syntheses"*ChemSusChem* **2014**, *7*, 999–1009.

[35] M. M. Titirici, R. J. White, N. Brun, V. L. Budarin, D. S. Su, F. del Monte, J. H. Clark, M. J. MacLachlan, "Sustainable carbon materials" *Chem. Soc. Rev.* **2015**, *44*, 250.

[36] W. Xu, E. I. Cooper, C. A. Angell, "Ionic Liquids: Ion Mobilities, Glass Temperatures, and Fragilities" *J. Phys. Chem. B* **2003**, *107*, 6170–6178

[37] M. C. Gutiérrez, M. L. Ferrer, C. R. Mateo, F. del Monte, "Freeze-Drying of Aqueous Solutions of Deep Eutectic Solvents: A Suitable Approach to Deep Eutectic Suspensions of Self-Assembled Structures" *Langmuir* **2009**, *25*, 5509–5515

[38] M. C. Gutiérrez, F. Rubio, F. del Monte, "Resorcinol-Formaldehyde Polycondensation in Deep Eutectic Solvents for the Preparation of Carbons and Carbon-Carbon Nanotube Composites" *Chem. Mater.* **2010**, *22*, 2711–2719

[39] M. C. Gutiérrez, M. L. Ferrer, L. Yuste, F. Rojo, F. del Monte, "Bacteria Incorporation in Deep-eutectic Solvents through Freeze-Drying" *Angew. Chem.* **2010**, *49*, 2158–2162.

[40] Y. Chen, Z. Chen, S. Xiao, H. Liu, "A novel thermal degradation mechanism of phenol–formaldehyde type resins" *Thermochim. Acta*, 2008, **476**, 39–43.

[41] P. Przybylski, G. Wojciechowski, B. Brzezinski, G. Zundel, F. Bartl, "FTIR studies of the interactions of 1,3,5-triazabicyclo[4.4.0]dec-5-ene with 4-tert-butylphenol and 4-cyanophenol" *J. Mol. Struct.* **2003**, *661-662*, 171–182.

[42] J.-H. Ha, K.-K. Lee, K.-H. Park, J.-H. Choi, S.-J. Jeon, M. Cho, "Integrated and dispersed photon echo studies of nitrile stretching vibration of 4-cyanophenol in methanol" *J. Chem. Phys.* **2009**, *130*, 204509.

[43] F. Lahmani, M. Broquier, A. Zehnacker-Rentien, "The **o**-cyanophenol dimer as studied by laser-induced fluorescence and IR fluorescence dip spectroscopy: a study of a symmetrical double hydrogen bond" *Chem. Phys. Lett.* **2002**, *354*, 337–348.

[44] I. L. Moudrakovski, C. I. Ratcliffe, J. A. Ripmeester, L. Q. Wang, G. J. Exarhos, T. F. Baumann, J. H. Satcher, "Nuclear Magnetic Resonance Studies of Resorcinol−Formaldehyde Aerogels." *J. Phys. Chem. B* **2005**, *109*, 11215–11222.

[45] S. Mulik, C. Sotiriou-Leventis, N. Leventis, "Time-Efficient Acid-Catalyzed Synthesis of Resorcinol− Formaldehyde Aerogels." *Chem. Mater.* **2007**, *19*, 6138–6144.

[46] K. Nakanishi and N. Soga, "Phase Separation in Silica Sol-Gel System Containing Poly(Ethylene oxide) II. Effects of Molecular Weight and Temperature" *Bull. Chem. Soc. Jpn.*, **1997**, *70*, 587–592.

[47] H. Kaji, K. Nakanishi, N. Soga, T. Inoue, N. Nemoto "In situ Observation of Phase Separation Processes in Gelling Alkoxy-Derived Silica System by Light Scattering Method" *J. Sol-Gel Sci Technol.* **1994**, *3*, 169–188.

[48] J. Renou, J. François-Rossetti, B. Imerick, "Étude des Solides Poreux, III. Isotherms D´Adsorption Irregulieres" *Bul. Soc. Chim. Fr.*, **1961**, 91, 446–450.

[49] A. Grosman, C. Ortega, "Cavitation in Metastable Fluids Confined to Linear Mesopores" *Langmuir* **2011**, 27, 2364–2374.

[50] P. Van Der Voort, P.I. Ravikovitch, K.P. de Jong, A.V. Neimark, A.H. Janssen, M. Benjelloun, E. van Bavel, P. Cool, B.M. Weychuysen, E.F. Vansant, "Plugged hexagonal templated silica: a unique micro- and mesoporous composite material with internal silica nanocapsules" *Chem. Commun.* **2002**, 9, 1010–1011.

[51] G. Rasines, C. Macias, M. Haro, J. Jagiello, C. O. Ania, "Effects of CO2 activation of carbon aerogels leading to ultrahigh micro-meso porosity", *Microp. Mesop. Mater.*, **2015**, 209, 18-22.

[52] F. Kapteijn, J. A. Moulijn, S. Matzner H.-P. Boechm, "The development of nitrogen functionality in model chars during gasification in CO_2 and O_2" *Carbon*, **1999**, *37*, 1143–1150.

[53] J. R. Pels, F. Kapteijn, J. A. Moulijn, Q. Zhu, K. M. Thomas, "Evolution of nitrogen functionalities in carbonaceous materials during pyrolysis" *Carbon*, **1995**, *33*, 1641–1653.

[54] C. Song, J. Zhang, "Electrocatalytic oxygen reduction reaction" in "PEM fuel cell electrocatalysts and catalysts layers: fundamentals and applications, vol. XXII." Editor: J. Zhang, Springer, **2008**, 89–134.

[55] M. Gara, K. R. Ward, R. G. Compton, "Nanomaterial modified electrodes: evaluating oxygen reduction catalysts" *Nanoscale* **2013**, *5*, 7304–7311.

[56] J. Masa, C. Batchelor-McAuley, W. Schuhmann, R. G. Compton, "Koutecky–Levich analysis applied to nanoparticle modified rotating disk electrodes: Electrocatalysis or misinterpretation?" *Nano Research.* **2014**, *7*, 71–78

[57] J. Liang, Y. Zheng, J. Chen, J. Liu, D. Hulicova-Jurcakova, M. Jaroniec, S. Z. Qiao, "Facile Oxygen Reduction on a Three-Dimensionally Ordered Macroporous Graphitic C_3N_4/Carbon Composite Electrocatalyst" *Angew. Chem. Int. Ed.* **2012**, *51*, 3892–3896

[58] S. Yang, L. Zhi, K. Tang, X. Feng, J. Maier, K. Müllen, "Efficient Synthesis of Heteroatom (N or S)-Doped Graphene Based on Ultrathin Graphene Oxide-Porous Silica Sheets for Oxygen Reduction Reactions" *Adv. Funct. Mater.* **2012**, *22*, 3634 –3640..

[59] J.-E. Park, Y. J. Jang, Y. J. Kim, M.-S. Song, S. Yoon, D. H. Kim, S.-J. Kim, "Sulfur-doped graphene as a potential alternative metal-free electrocatalyst and Pt-catalyst supporting material for oxygen reduction reaction" *Phys. Chem. Chem. Phys.* **2014**, *16*, 103–109.

[60] N. Brun, S. A. Wohlgemuth, P. Osiceanu, M. M. Titirici, "Original design of nitrogen-doped carbon aerogels from sustainable precursors: application as metal-free oxygen reduction catalysts" *Green Chem.* **2013**, *15*, 2514–2524.

[61] J. Liang, Y. Jiao, M. Jaroniec, S. Z. Qiao, "Sulfur and Nitrogen Dual-Doped Mesoporous Graphene Electrocatalyst for Oxygen Reduction with Synergistically Enhanced Performance" *Angew. Chem. Int. Ed.* **2012**, *51*, 11496–11500.

[62] H. Estrade-Szwarckopf, "XPS photoemission in carbonaceous materials: A "defect" peak beside the graphitic asymmetric peak" *Carbon* **2004**, *42*, 1713–1721.

[63] F. Rouquerol, J. Rouquerol, K.S.W. Sing, P. Llewellyn, G. Maurin, "Adsorption by Powders and Porous Solids", 1st ed., Elsevier **2014**.

[64] J. Jagiello, J.P. Olivier, "Carbon slit pore model incorporating surface energetical heterogeneity and geometrical corrugation", *Adsorpt.* **2013**, 19, 777–783.

Figure 1 – DSC scans of R2CPC-DES and R4CPC-DES.

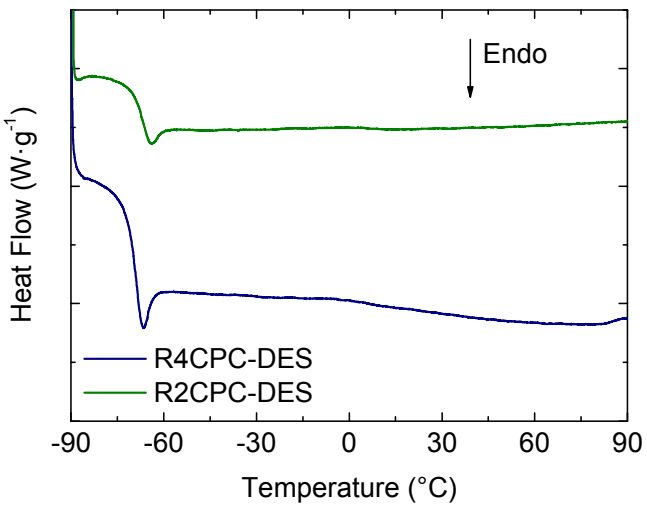

Figure 2 – FTIR spectra of (a) R2CPC and (b) R4CPC resins.

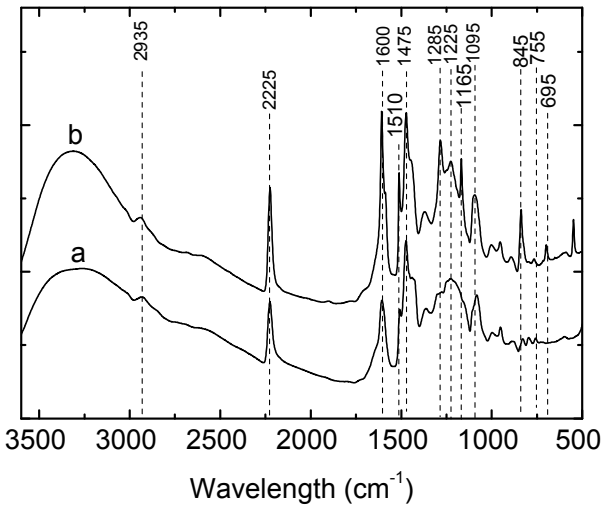

Figure 3 – Solid state ^{13}C CPMAS NMR of (a) R2CPC and (b) R4CPC resins.

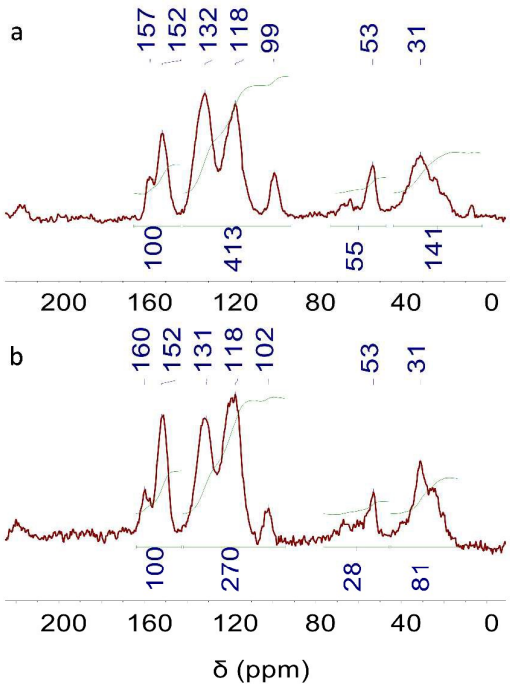

Figura 4 – SEM micrographs of (top panel) R2CPC and R4CPC resins, and (bottom panel) R2CPC and R4CPC carbons. Bars are 5 μm.

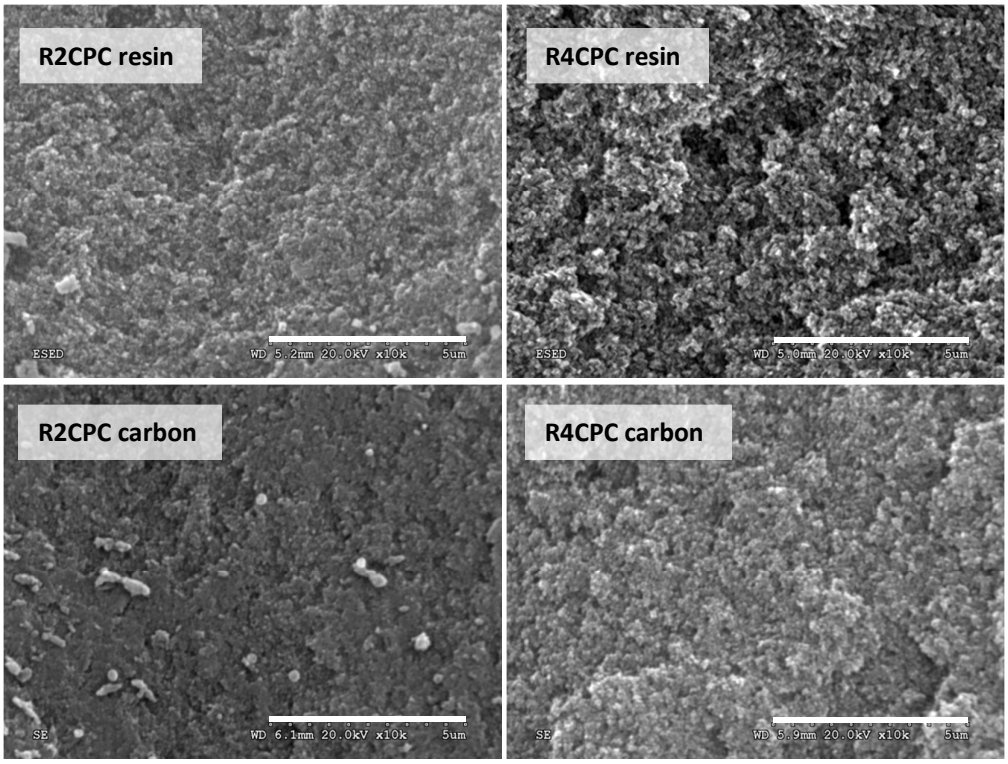

Figure 5 – Textural properties of R2CPC and R4CPC carbons; (a) N_2 adsorption/desorption isotherms at –196 °C, (b) CO_2 adsorption isotherms at 0 °C, and (c) pore size distribution obtained from 2D-NLDFT-HS.

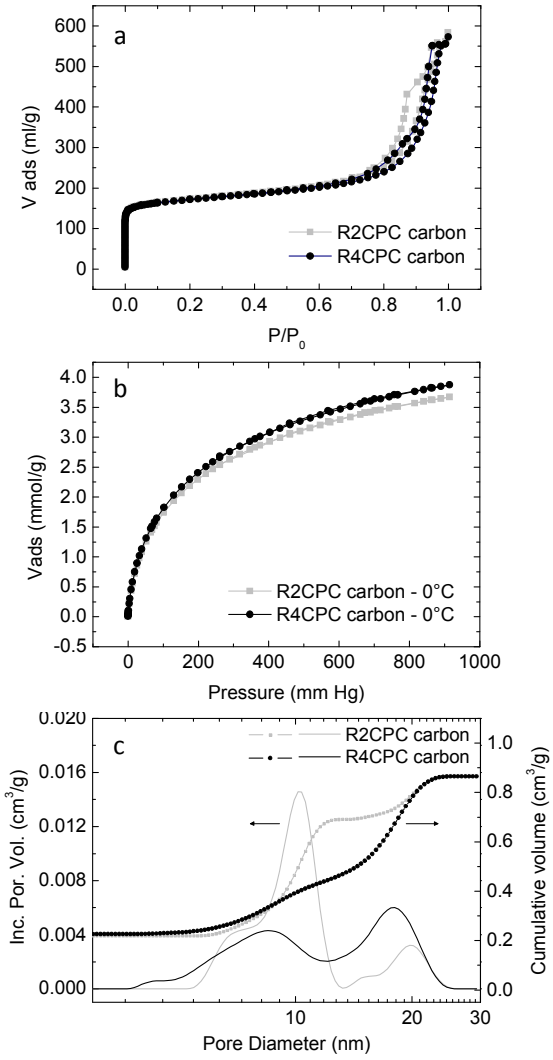

Figure 6 – XPS N1s deconvoluted spectra of R2CPC (top) and R4CPC (bottom) carbons.

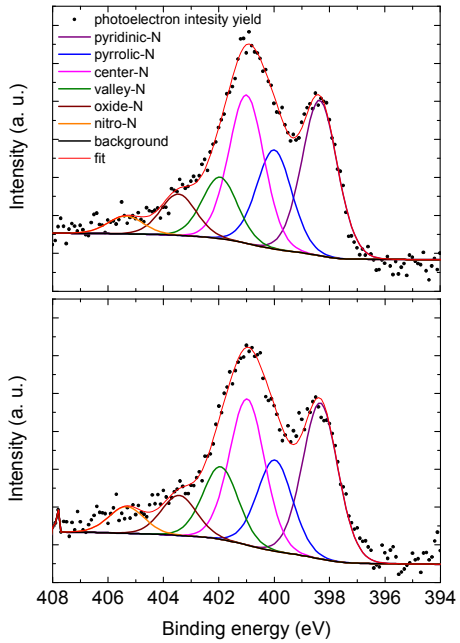

Figure 7 – CV of (a) R2CPC and (b) R4CPC carbons in N_2 saturated 0.1 M KOH (black line) and O_2 saturated 0.1 M KOH (color line). LSV curves recorded at different rotation speeds of (c) R2CPC and (d) R4CPC carbons in O_2 saturated 0.1M KOH.

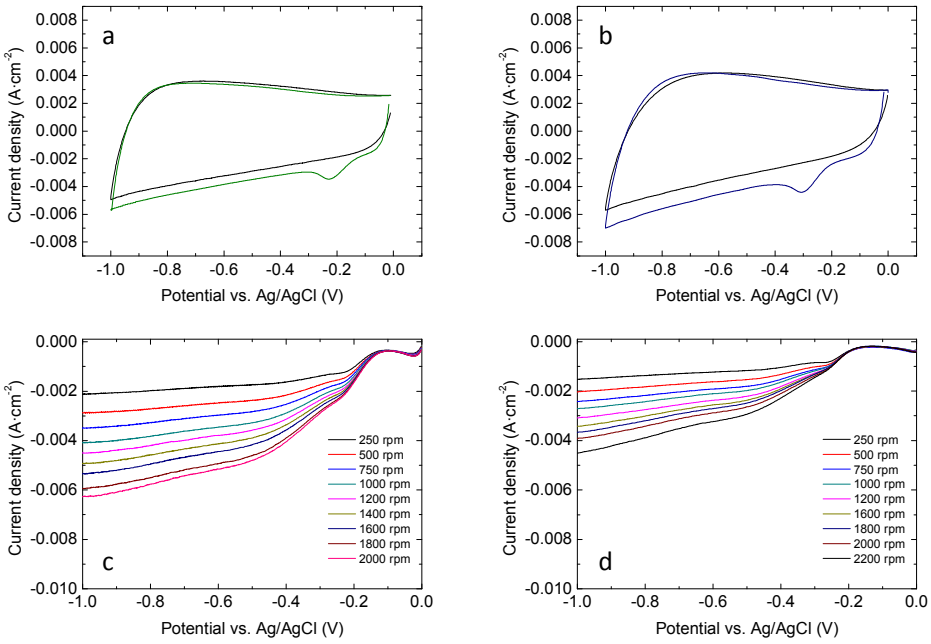

Figure 8 – (a) LSV curves at 2000 rpm of R2CPC and R4CPC carbons. The PSV curve of Pt/C is also included for comparison. (b) K-L lines of R2CPC and R4CPC carbons. The K-L line of Pt/C 20% at -250 mV is also included for comparison. (c) Plot representing the number of transferred electrons provided by every sample at different potentials. (d) Stability of the R4CPC carbon over time and methanol crossover. The methanol crossover of Pt/C 20% is also included for comparison.

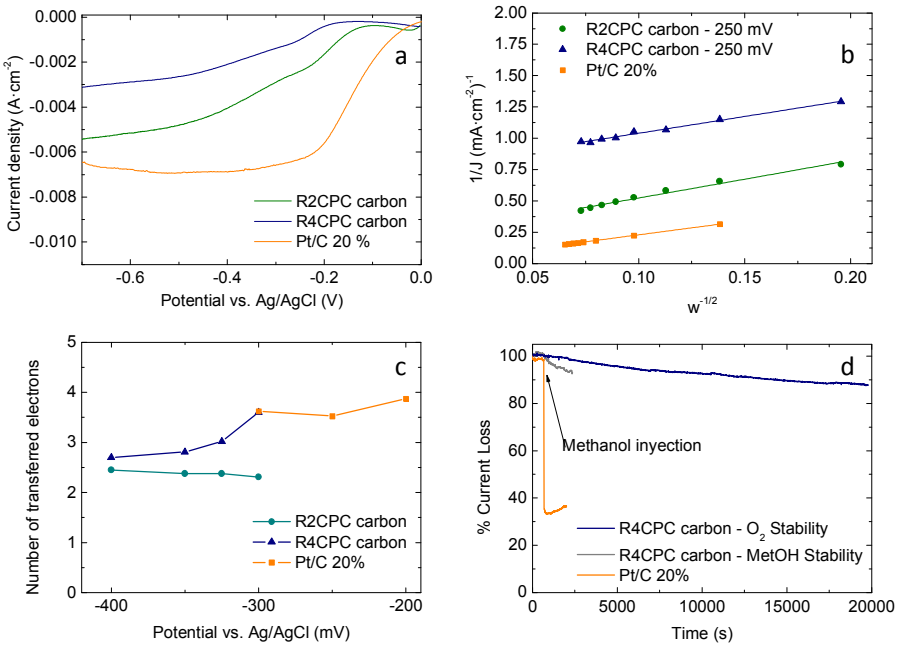

Table 1 – Chemical composition of R2CPC and R4CPC carbons obtained from either XPS ([a]) and ECA ([b]). Table includes the theoretical nitrogen content ([c]) and the carbon conversion of both samples.

	Chemical content[a] (at%)			Chemical content[b] (wt%)		N content[c] (wt%)	Carbon conversion (wt%)
	C_{XPS}	O_{XPS}	N_{XPS}	C_{ECA}	N_{ECA}		
R2CPC	91.3	6.6	2.1	90.02	2.31	8.2	69
R4CPC	93.3	5.0	1.7	90.98	2.40	8.2	62

Table 2 – Textural data obtained from N_2 adsorption/desorption isotherms at –196 °C and CO_2 adsorption isotherms at 0 °C of R2CPC and R4CPC carbons.

	N_2 adsorption						CO_2 adsorption	
	S_{BET}[a] m^2/g	V_{total}[b] cm^3/g	$V_{micropores}$[c] cm^3/g	$V_{mesopores}$[c] cm^3/g	$W_{o,N2}$[d] cm^3/g	L_{N2}[e] (nm)	$W_{o,CO2}$[d] (cm^3/g)	L_{CO2}[e] (nm)
R2CPC	668	0.866	0.214	0.633	0.239	0.66	0.271	0.55
R4CPC	660	0.859	0.218	0.629	0.242	0.64	0.272	0.55

[a] Obtained after the application of the BET equation to the N_2 adsorption/desorption isotherms; [b] Total pore volume calculated at $p/p_0 \sim 0.99$; [c] Pore volumes calculated using the 2-NLDFT-HS method; [d] Micropore volume calculated using the Dubinin–Radushkevich equation; [e] Average micropore size calculated using the Stoeckli-Ballerini equation.

Table 3 – Binding energies (eV) and contributions (%) of the different types of nitrogen as obtained from XPS N1s core levels of R2CPC and R4CPC carbons.

	Binding energy (eV) – Area (%)	
Type of Nitrogen	**R2CPC**	**R4CPC**
Pyridinic-N	398.36 – 32.9	398.34 – 39.9
Pyrrolic-N	400.00 – 21.0	399.98 – 18.1
Quaternary-N_{center}	401.00 – 31.5	400.98 – 29.0
Quaternary-N_{valley}	401.96 – 7.37	401.94 – 14.4
Oxide-N	403.46 – 4.96	403.44 – 4.50
Nitro-N	405.36 – 2.14	405.34 – 3.00